

Unified Phase-Field Framework for Antiferroelectric, Ferroelectric and Dielectric Phases: Application to HZO Thin Films

P. Pankaj¹, Sandeep Sugathan¹, Si Joon Kim², Pil-Ryung Cha^{1,*}

¹School of Materials Science and Engineering, Kookmin University, Seoul 02707, Republic of Korea

²Department of Electrical and Electronics Engineering, Kangwon National University, Chuncheon, Gangwon-Do 24341, Republic of Korea

*Corresponding author: cprdream@kookmin.ac.kr

Abstract

Polycrystalline hafnia-based thin films exhibit mixed ferroelectric (FE), antiferroelectric (AFE), and dielectric (DE) behavior, with switching characteristics strongly influenced by microstructure and phase distribution. Here, we develop a unified grain-resolved three-dimensional phase-field framework for metal–insulator–metal capacitors that simultaneously captures ferroic phase characteristics in realistic polycrystalline microstructures by explicitly incorporating grain topology and crystallographic orientation. Antipolar sublattice kinetics are represented via the coupled evolution of macroscopic and staggered polarization order parameters. All thermodynamic and kinetic parameters are calibrated to experimental P – E hysteresis loops and held fixed across all simulations. The results show that phase fractions primarily determine hysteresis character, while vertical segregation of AFE- and FE-rich regions systematically reduces the effective coercive field (E_c) under identical electrical loading. Grain-resolved analysis reveals that this reduction arises from microstructure-assisted switching pathways and electrostatic coupling between layers. These findings demonstrate that vertical phase arrangement provides a viable strategy to engineer switching behavior in hafnia-based ferroic capacitors and highlight the importance of explicit microstructural resolution for quantitative phase-field modeling.

Keywords: Hafnia-based thin films; AFE–FE switching; Grain-resolved phase-field modeling; Polycrystalline films; Coercive field

1 Introduction

Antiferroelectric (AFE) and ferroelectric (FE) materials are actively explored for applications spanning nonvolatile memories, negative-capacitance devices, and high-power energy-storage capacitors, owing to their rich electric-field-driven phase transitions and hysteretic responses [1, 2, 3, 4, 5]. In particular, the hallmark double-hysteresis response of AFEs enables large recoverable energy density and fast charge–discharge operation, and has also been linked to electrocaloric and resistive-memory functionalities [1, 2, 4]. In hafnia-based systems, HfO_2 - and $\text{Hf}_x\text{Zr}_{1-x}\text{O}_2$ -based thin films have emerged as technologically relevant platforms compatible with CMOS processing, exhibiting ferroelectric, antiferroelectric-like, and dielectric behavior depending on composition, thickness, and processing conditions [6, 7, 8, 5]. Notably, AFE-like $\text{ZrO}_2/\text{HfO}_2$ stacks have been proposed to mitigate the voltage-scaling and cycling-lifetime limitations associated with high- E_c FE hafnia, while enabling memory-relevant switching concepts and high-efficiency energy storage [3]. Together, these studies highlight the central challenge in antiferroelectric and ferroelectric device design: achieving reduced switching fields and controlled hysteresis characteristics without sacrificing reversibility or endurance.

In hafnia-based films, AFE-like switching is often interpreted primarily in terms of electric-field-induced crystallographic phase transitions between nonpolar and polar phases, with the critical switching field governed by relative phase energetics rather than explicit antipolar domain ordering [9, 10]. In contrast, studies on Pb-based perovskite antiferroelectrics have demonstrated that deliberately disrupting long-range antipolar order—through entropy-driven disorder, grain refinement, antipolar frustration, or engineered polarization heterogeneity—can diffuse the AFE–FE transition, reshape hysteresis behavior, and enhance functional performance [11, 12, 13, 14]. In such systems, depolarization fields and

electrostatic boundary conditions play a central role in determining the reversibility and stability of field-induced phase transitions [15].

Experimentally, hafnia-based thin films exhibit a wide spectrum of switching responses, ranging from FE-like single hysteresis loops to AFE-like double loops and nearly linear dielectric behavior, reflecting strong sensitivity to phase fraction, microstructure, and cycling history [8, 7]. Notably, polarization cycling in $\text{Hf}_x\text{Zr}_{1-x}\text{O}_2$ films can induce a systematic evolution of AFE hysteresis, in which initially separated sub-loops progressively merge into a single loop with finite remanent polarization while retaining exceptionally high endurance [16]. From a device perspective, these observations reveal a fundamental trade-off in hafnia-based memories: FE-rich films provide finite P_r but typically require relatively high switching fields and exhibit pronounced cycling sensitivity, whereas AFE-rich films exhibit highly reversible switching with near-zero P_r . This trade-off motivates strategies to reduce the effective coercive field E_c while preserving FE-like hysteresis characteristics, without relying on chemistry- or defect-driven phase stabilization.

Phase-field modeling has played a central role in elucidating FE and AFE switching mechanisms, including domain formation, hysteresis evolution, and phase competition. Unified multi-domain phase-field frameworks capable of simulating coexisting FE, AFE, and dielectric regions in hafnia-based films have been reported and successfully used to reproduce mixed hysteresis behavior and cycling trends [17, 18]. However, in most such models, polycrystallinity is represented through grid-wise phase mixtures or reduced-dimensional geometries, rather than an explicit three-dimensional (3-D) grain-resolved microstructure. As a result, these approaches are limited in their ability to isolate how realistic grain connectivity, vertical phase arrangement, and grain-scale electrostatic coupling govern the practical trade-off between reducing E_c and retaining FE-like P_r in polycrystalline capacitors. At the same time, experimental and atomistic studies suggest that confinement-driven grain energetics and interface-related effects strongly influence phase stability in ZrO_2/HZO , promoting stabilization of the orthorhombic phase and reshaping the free-energy landscape under applied electric fields [6, 7, 19, 20].

In this work, we address these gaps by developing a unified grain-resolved 3-D phase-field model for polycrystalline hafnia-based thin films. The model explicitly resolves polycrystallinity using a 3-D Voronoi grain topology with layer-resolved vertical phase assignment and evolves both P_m and P_s , enabling direct representation of antipolar sublattice kinetics. A uniaxial switching formulation appropriate for metal-insulator-metal capacitors is employed, in which nonlinear polarization instabilities are confined to the film-normal direction while depolarization fields are treated self-consistently through Poisson coupling with phase-dependent dielectric permittivity. This framework enables systematic investigation of how vertical phase arrangement and grain-scale electrostatic coupling influence switching pathways and control E_c and P_r in polycrystalline hafnia films under identical electrical loading.

2 Phase-field modeling framework and thermodynamic description

We employ a 3-D phase-field framework to simulate electric-field-driven switching in hafnia-based polycrystalline thin films containing AFE, FE, and DE grains. Polycrystallinity is represented by a fixed 3-D grain structure in which each grain is assigned a phase identity and a crystallographic orientation specified by the ZXZ Euler-angle convention; details of microstructure generation are provided in Section 4.2. The total free-energy of the polycrystalline film is given by

$$F = \int_V (f_{\text{bulk}} + f_{\text{grad}} + f_{\text{elc}} + f_{\text{elas}} + f_{\text{ap}}) dV. \quad (1)$$

where f_{bulk} describes the thermodynamics of AFE, FE, and DE grains, f_{grad} penalizes spatial variations of the polarization fields, f_{elc} accounts for long-range electrostatic interactions and depolarization fields, f_{elas} represents elastic energy, and f_{ap} represents coupling to the applied electric field.

2.1 Bulk thermodynamics and gradient energy

The bulk thermodynamics is described using the Kittel two-sublattice model [21, 22],

$$f_{\text{bulk}}(P_a, P_b) = \frac{\alpha(T)}{2}(P_a^2 + P_b^2) + \frac{\beta}{4}(P_a^4 + P_b^4) + \frac{\gamma}{6}(P_a^6 + P_b^6) + g P_a P_b, \quad (2)$$

where α, β, γ, g are the Landau coefficients, P_a and P_b denote the two-sublattice polarization. Introducing the macroscopic and staggered order parameters $P_m = P_a + P_b$ and $P_s = P_a - P_b$, and assigning material

parameters on a grain-by-grain basis, with $\mathcal{P}(k) \in \{\text{AFE}, \text{FE}, \text{DE}\}$ denoting the phase identity of grain k , the bulk free-energy density is expressed in the local crystallographic frame of grain k as [23]

$$f_{\text{bulk}}^{L,k}(\mathbf{P}_m, \mathbf{P}_s) = \frac{\alpha^{\mathcal{P}(k)}(T)}{4} [(P_m^L)^2 + (P_s^L)^2] + \frac{\beta^{\mathcal{P}(k)}}{32} [(P_m^L)^4 + 6(P_m^L)^2(P_s^L)^2 + (P_s^L)^4] \\ + \frac{\gamma^{\mathcal{P}(k)}}{192} [(P_m^L)^6 + 15(P_m^L)^4(P_s^L)^2 + 15(P_m^L)^2(P_s^L)^4 + (P_s^L)^6] + \frac{g^{\mathcal{P}(k)}}{4} [(P_m^L)^2 - (P_s^L)^2], \quad (3)$$

where the superscript L denotes the local crystallographic frame and $\alpha(T) = g + \alpha_0(T - T_0)$. Within this formulation, AFE, FE, and paraelectric states correspond to $P_m = 0$, $P_s = 0$, and $P_m = P_s = 0$, respectively [21, 24].

Experimental studies on orthorhombic HZO and ZrO_2 thin films under metal–insulator–metal capacitor boundary conditions show that polarization switching is predominantly confined to the film-normal direction [6, 7]. Although the film is 3-D and polycrystalline, texture analysis and wake-up-induced polar-axis reorientation indicate a primarily out-of-plane ferroelectric response [25]. Consequently, only the z -component of polarization is treated as switchable in this work, whereas transverse components are treated as non-switching contributions through an effective local dielectric stiffness χ_f . Suppressing the explicit grain index for notational simplicity, the local bulk free-energy density reduces to

$$f_{\text{bulk}}^L(\mathbf{P}_m, \mathbf{P}_s) = \frac{\alpha(T)}{4} [(P_{m,z}^L)^2 + (P_{s,z}^L)^2] + \frac{\beta}{32} [(P_{m,z}^L)^4 + 6(P_{m,z}^L)^2(P_{s,z}^L)^2 + (P_{s,z}^L)^4] \\ + \frac{\gamma}{192} [(P_{m,z}^L)^6 + 15(P_{m,z}^L)^4(P_{s,z}^L)^2 + 15(P_{m,z}^L)^2(P_{s,z}^L)^4 + (P_{s,z}^L)^6] + \frac{g}{4} [(P_{m,z}^L)^2 - (P_{s,z}^L)^2] \\ + \frac{1}{2\chi_f} \sum_{i=x,y} [(P_{m,i}^L)^2 + (P_{s,i}^L)^2]. \quad (4)$$

The gradient energy density is written in the global frame as

$$f_{\text{grad}}^G(\mathbf{P}_m) = \frac{G_{11}}{2} \sum_{i=x,y,z} [(\nabla P_{m,i}^G)^2 + (\nabla P_{s,i}^G)^2], \quad (5)$$

where G_{11} denotes isotropic gradient-energy coefficient, the superscript G denotes the global crystallographic frame.

2.2 Electrostatics and applied-field coupling

Electrostatic interactions arising from spatial variations of the macroscopic polarization are described by the energy density

$$f_{\text{elc}}^G(\mathbf{P}_m, \phi) = -\frac{1}{2} E_i^G P_{m,i}^G, \quad (6)$$

where the internal electric field is defined by $\mathbf{E}^G = -\nabla\phi^G$, with ϕ^G denoting the electrostatic potential. In the absence of free charges, electrostatic equilibrium requires $\nabla \cdot \mathbf{D}^G = 0$, which leads to the Poisson equation

$$(\varepsilon_{ij}\phi_{,j}^G)_{,i} = \frac{P_{m,i,i}^G}{\varepsilon_0}. \quad (7)$$

Here, $\varepsilon_{ij}(\mathbf{r}) = \varepsilon_r^\alpha \delta_{ij}$ denotes the phase-dependent isotropic relative permittivity, and ε_0 is the vacuum permittivity. Eq. (7) is solved using a conjugate-gradient method with a Jacobi preconditioner, subject to periodic in-plane and Dirichlet boundary conditions along the film normal.

The parameter χ_f represents a local dielectric stiffness entering only through the bulk free-energy functional as a harmonic penalty on polarization, whereas the relative dielectric permittivity tensor ε_{ij} appears only in Poisson's equation and governs long-range electrostatic screening. These contributions are therefore treated independently to avoid double counting of dielectric response, as discussed in analyses separating bulk and depolarization-field contributions to small-signal capacitance [26].

The energetic contribution of an externally applied electric field is

$$f_{\text{ap}}^G(\mathbf{P}_m) = -E_{\text{ap},i}^G P_{m,i}^G, \quad (8)$$

which reduces to $f_{\text{ap}}^G = -E_{\text{ap},z}^G P_{m,z}^G$ under out-of-plane capacitor loading. Field-induced modification of AFE order occurs indirectly through $P_{m,z}$ rather than via a direct linear coupling to the staggered order parameter [27].

Elastic energy is neglected in the present formulation as our focus is to isolate electrostatic, microstructural, and phase-fraction effects on polarization switching in polycrystalline hafnia thin films. The Landau coefficients are calibrated directly against experimental P - E hysteresis loops of comparable thin-film geometry (see Section 3.2); thus, the resulting effective bulk free-energy landscape implicitly reflects the average elastic constraints associated with substrate clamping and processing-induced residual stresses. Also, previous phase-field studies indicate that elastic coupling exerts only a secondary influence on the macroscopic hysteresis response relative to electrostatic interactions and domain-wall energetics [28, 29].

2.3 Phase-transition thermodynamics

The AFE–FE transition in HZO-based systems is dominated by polarization along the polar crystallographic axis. Transverse components respond predominantly linearly to the applied field and are incorporated through an effective dielectric stiffness χ_f . Accordingly, only the polar (z -axis) components are retained in describing the transition thermodynamics. Under this approximation, Eq.(4) can be expressed in terms of an effective scalar order parameter P :

$$F(P) = \frac{1}{2}a(T)P^2 + \frac{1}{4}bP^4 + \frac{1}{6}cP^6, \quad (9)$$

where P denotes $P_{s,z}^L$ for the AFE mode or $P_{m,z}^L$ for the FE mode, with $b = \beta/8$ and $c = \gamma/32$. The temperature-dependent quadratic coefficients are

$$\begin{aligned} a_s(T) &= \frac{\alpha(T) - g}{2} = \frac{\alpha_0}{2}(T - T_0), & \text{AFE}, \\ a_m(T) &= \frac{\alpha(T) + g}{2} = \frac{\alpha_0}{2}\left(T - T_0 + \frac{2g}{\alpha_0}\right), & \text{FE}, \end{aligned} \quad (10)$$

yielding instability temperatures $T_s^* = T_0$ and $T_m^* = T_0 - 2g/\alpha_0$. The coupling parameter g therefore shifts the FE instability downward relative to the AFE branch.

At high temperature ($a > 0$), the system is paraelectric (PE) with a single minimum at $P = 0$. Upon cooling, the free-energy landscape evolves into a *triple-well* form, marked by the appearance of two metastable polar minima while the central paraelectric minimum remains globally stable. This is characterized by the *ordered spinodal*, $a_{ord}^{spn} = b^2/(4c)$. At coexistence, $a_{coex} = 3b^2/(16c)$, where paraelectric and polar states are degenerate. Further cooling removes the central minimum at the disordered spinodal $a = 0$, leaving a stable double-well profile. The free-energy landscapes are shown in Fig. 1.

The presence of an intermediate triple-well free-energy landscape provides the fundamental thermodynamic distinction between AFE double hysteresis and FE single hysteresis: in AFE systems, a low-field nonpolar minimum enables reversible field-induced switching, whereas FE systems exhibit a stable double-well potential supporting spontaneous polarization. This interpretation is consistent with Landau stability analyses and Gibbs free-energy reconstructions of AFE switching [23, 30, 31]. Pulsed measurements in ZrO_2 further suggest that AFE–FE switching dynamically traverses spinodal-bounded unstable regions [32], corresponding to loss of local stability of the uniform polarization state [33].

For $g > 0$, the AFE branch softens first, producing a triple-well landscape and characteristic AFE double hysteresis. For $g < 0$, the FE branch dominates, and the system exhibits a spontaneous double-well state and single hysteresis loop. Accordingly, the dominant instability pathway is

$$a(T) = \begin{cases} a_s(T), & g > 0 \quad (\text{AFE-dominated}), \\ a_m(T), & g < 0 \quad (\text{FE-dominated}). \end{cases} \quad (11)$$

Experimental studies have reported that electric-field-induced AFE–FE switching is first-order, characterized by discontinuous polarization and hysteresis [34]. To obtain triple-well regime in second-order formulation, it is required to eliminate the antipolar order parameter via its stationary condition [17]. However, this enforces instantaneous equilibration and removes it as an independent field. Consequently, finite-rate relaxation, spatial pinning, and domain-wall energetics of P_s cannot be captured, and the kinetic pathways by which antipolar order evolves during field-driven switching remain inaccessible. The need for explicit evolution of P_s is reinforced by sublattice-resolved analyses of polarization switching in hafnia-based AFE [35]. We therefore adopt a first-order free-energy description with explicit antipolar kinetics, consistent with classical Pb-based AFE systems [34, 36].

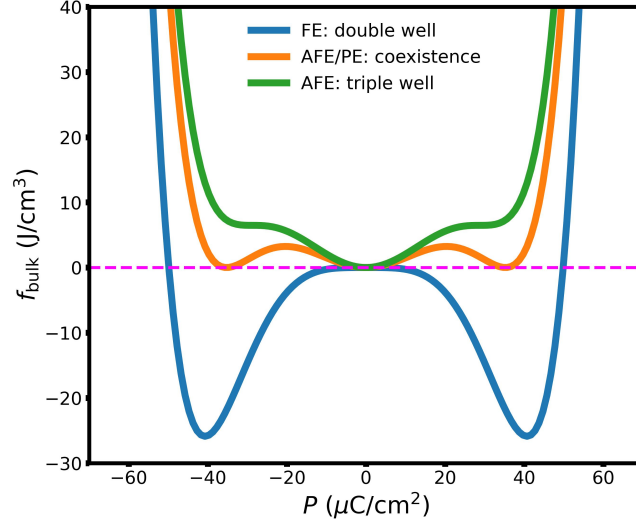


Figure 1: Zero-field bulk free-energy density $f(P)$ versus polarization P for the scalar Kittel–Landau model. Curves correspond to FE double-well ($a < 0$), AFE/PE coexistence ($a = a_{\text{coex}}$), and AFE triple-well ($a_{\text{ord}}^{\text{spn}} > a > a_{\text{coex}}$).

2.4 Kinetic evolution

While f_{bulk}^L is evaluated in the local crystallographic frame of each grain, all other energy contributions are evaluated in the global frame. The two frames are related by $\mathbf{P}^L = \mathbf{R}\mathbf{P}^G$:

$$\frac{\delta F}{\delta \mathbf{P}^G} = \mathbf{R}^\top \frac{\delta F}{\delta \mathbf{P}^L}. \quad (12)$$

Here, \mathbf{R} denotes the orthogonal rotation matrix that transforms polarization vectors from the global to the local crystallographic frame of each grain.

The domain evolution within each grain is described by TDGL equations:

$$\frac{\partial P_{m,i}^G}{\partial t} = -\Gamma \frac{\delta F}{\delta P_{m,i}^G}, \quad \frac{\partial P_{s,i}^G}{\partial t} = -\Gamma \frac{\delta F}{\delta P_{s,i}^G}, \quad i \in \{x, y, z\}. \quad (13)$$

where Γ is the kinetic coefficient.

All governing equations are expressed in nondimensional form using characteristic reference scales; details are provided in Section 1 of the Supplementary Information.

3 Experimental methods and parameter calibration

3.1 Experimental method

Ferroelectric TiN/Hf_{0.5}Zr_{0.5}O₂/TiN and antiferroelectric TiN/ZrO₂/TiN capacitors were fabricated on p-type Si substrates. A 300-nm-thick SiO₂ layer was thermally grown on the substrates prior to device fabrication. TiN bottom electrodes (~90 nm) were deposited at room temperature by RF sputtering. Hf_{1-x}Zr_xO₂ ($x = 0.5, 1$) thin films were deposited by atomic layer deposition (ALD) at 250 °C using Hf[N(CH₃)₂]₄ (TDMA-Hf), Zr[N(CH₃)₂]₄ (TDMA-Zr), and O₃ as the Hf precursor, Zr precursor, and oxygen source, respectively, with a growth rate of ~0.2 nm/cycle. The Zr composition was controlled by the ALD cycle ratio, and the total number of cycles was adjusted to achieve a uniform film thickness of ~10 nm. After Hf_{1-x}Zr_xO₂ deposition, TiN top electrodes (~90 nm) were deposited by RF sputtering under the same conditions as the bottom electrodes. The samples were then annealed by rapid thermal annealing (RTA) at 400 °C for 60 s under N₂ atmosphere. TiN top electrodes were patterned using photolithography and wet etching with a Pd/Au hard mask. Electrical properties were characterized by P – E hysteresis measurements using a semiconductor parameter analyzer (Keithley 4200A-SCS) equipped with a pulse measurement unit (4225-PMU) at 10 kHz. Prior to measurement, all devices were subjected to 10⁵ wake-up cycles under an electric field of 3 MV/cm to stabilize the FE and AFE responses.

3.2 Parameter Calibration

For the simulations, experimentally relevant electric-field loading conditions are reproduced using a triangular electric-field waveform with frequency $\nu = 10$ kHz and peak amplitude 3 MV/cm applied across a 10 nm-thick film. Additional numerical details of the sweep-rate implementation, including discretization parameters and timestep considerations, are provided in Section 2 of the Supplementary Information.

The Landau coefficients and selected kinetic parameters are calibrated against experimental P – E hysteresis loops measured on polycrystalline HZO and ZrO_2 thin films, while the remaining kinetic parameters are adopted from established literature. Fig. 2 compares the calibrated TDGL responses with the corresponding experimental data, and the fitted coefficients are summarized in Table 1. Detailed analysis of microstructural domain evolution is deferred to the polycrystalline simulations discussed in Section 4.3. The calibrated parameters, electric-field increments, and temporal discretization are treated as intrinsic and kept fixed for all simulations. Next, we first establish the ideal AFE single-crystal thermodynamic limit from equilibrium solutions and then introduce spatially uniform TDGL kinetics to elucidate the origin of double hysteresis. Finally, the framework is extended to fully 3-D grain-resolved polycrystalline films to examine the influence of single-layer and multilayer architectures on E_c and P_r .

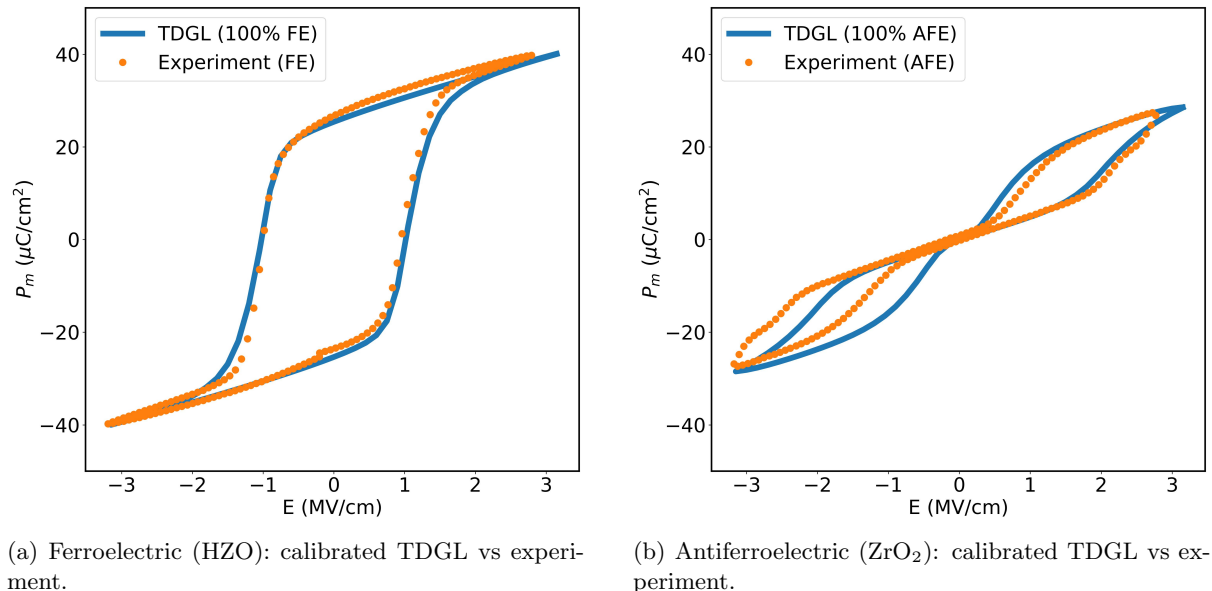


Figure 2: Calibration of thermodynamic and kinetic parameters using experimental P – E hysteresis loops of polycrystalline thin films. Solid lines denote TDGL simulations and dashed lines experimental data, obtained under identical electric-field loading conditions.

4 Results and discussion

4.1 Intrinsic switching response in single-crystal film

In this section, we analyze the ideal single-crystal response under quasi-static electric-field loading to establish the intrinsic thermodynamic switching pathway prior to introducing kinetic effects. Equilibrium polarization states are obtained by minimizing Eq. (3) using a Newton–Raphson scheme:

$$\frac{\partial f_{bulk}^L}{\partial P_m^L} = 0, \quad \frac{\partial f_{bulk}^L}{\partial P_s^L} = 0, \quad (14)$$

This procedure traces stable and metastable free-energy minima, and results in a sharp, discontinuous double hysteresis loop as shown in Fig. 3(red-blue). At zero applied electric field, the system adopts an antipolar equilibrium state with $P_m \approx 0$ and two degenerate minima $P_s = \pm P_{s0} \approx \pm 40.9 \mu\text{C}/\text{cm}^2$. As the field increases from zero, antipolar order destabilizes until a discontinuous AFE→FE transition collapses P_s to zero, producing a field-induced polar state with $P_{m0} \approx 40 \mu\text{C}/\text{cm}^2$. Upon field reversal at $E = 0$, restoration of antipolar order reproduces the double hysteresis loop. This behavior represents

Table 1: Calibrated material, kinetic, and geometric parameters.

Parameter	AFE (ZrO ₂)	FE (HZO)	DE [†]
α (J m C ⁻²)	5.022×10^8	-2.98×10^8	9.5×10^9
β (J m ⁵ C ⁻⁴)	-9.065×10^{10}	-8.520×10^9	0
γ (J m ⁹ C ⁻⁶)	2.190×10^{12}	3.134×10^{11}	0
g (J m C ⁻²)	5.453×10^8	-2.484×10^8	0
χ_f (C ² J ⁻¹ m ⁻¹)	5.0×10^{-10}	5.0×10^{-10}	2.1×10^{-10} ^[28]
G_{11} (J m ³ C ⁻²)	1.0×10^{-9}	5.066×10^{-10} ^[28]	2.5×10^{-9}
Γ (C ² J ⁻¹ m ⁻¹ s ⁻¹)	0.2	0.833 ^[37]	1
ε_r	40 ^[38, 39]	30 ^[29, 38, 39]	15 ^[38, 39]
<i>Geometric and microstructural parameters</i>			
Thin-film surface area ($n_x \times n_y$)	940×940 nm ²		
Thin-film thickness (t_z)	10 nm		
Number of grains	800		
Δh	1 nm		
Δt	0.06 ns		

[†] For the DE phase, the parameters α and χ_f are chosen such that $\alpha/4 = 1/(2\chi_f)$, yielding an isotropic linear dielectric response with no spontaneous polarization. Higher-order Landau coefficients (β , γ , g) are therefore set to zero.

the ideal thermodynamic limit of AFE switching and is consistent with experimental observations in epitaxial Pb-based AFE systems [40].

We next examine kinetic effects by evolving the same system using the TDGL equations and comparing the trajectories with the equilibrium reference. The macroscopic polarization is obtained by spatially averaging $P_{m,z}$ over the simulation domain [41]. Fig. 3 shows the crossover from dynamic to quasi-static switching. At the experimental sweep rate ($\nu = 10$ kHz, black), the response deviates from equilibrium near $E \approx 0$ because antipolar order does not fully recover, reflecting kinetic limitations rather than thermodynamic instability. Reducing the sweep rate progressively restores the equilibrium pathway: at intermediate rates (green), antipolar order fully re-emerges at zero field with $\pm P_s$ domains, while sufficiently slow sweeping (yellow) drives convergence to the quasi-static thermodynamic limit with a sharp symmetric P - E loop. Continued coarsening in this single-crystal setting can bias the system toward a single-variant P_s domain, reflecting kinetic selection in the absence of thermal fluctuations or microstructural disorder. Microstructures at characteristic field states for green-curve are shown in Fig. S1.

These results show that TDGL dynamics capture the crossover from kinetically limited switching at experimentally relevant sweep rates to the quasi-static thermodynamic limit. The experimentally calibrated field evolution is therefore retained to maintain realistic switching conditions, while the quasi-static electric-field loading serves only as a thermodynamic reference.

4.2 Polycrystalline thin-film microstructures and architecture design

To examine the influence of microstructure on AFE–FE switching, the single-crystal framework is extended to polycrystalline thin films. 3-D polycrystalline geometries are generated using Voronoi tesselation, producing a grain-resolved topology with sharp, immobile grain boundaries. Grain assignment is based on spatial proximity in all three dimensions, yielding equiaxed rather than columnar grains. In multilayer architectures, grains are confined within individual layers and do not span layer interfaces. Material phase identity is assigned on a grain-by-grain basis, consistent with grain-scale control of phase stability in HZO systems [19]. Representative polycrystalline microstructures used in the TDGL simulations are shown in Fig. 4.

The resulting grain-resolved structure introduces strong spatial heterogeneity in crystallographic orientation and material parameters. Each grain retains its assigned phase that determines its local Landau coefficients, dielectric response, and kinetic prefactor. While the polarization field remains continuous across grain boundaries, discontinuities in material parameters give rise to spatially varying switching barriers and coercive fields. Consequently, switching proceeds non-uniformly, with domain walls pinning

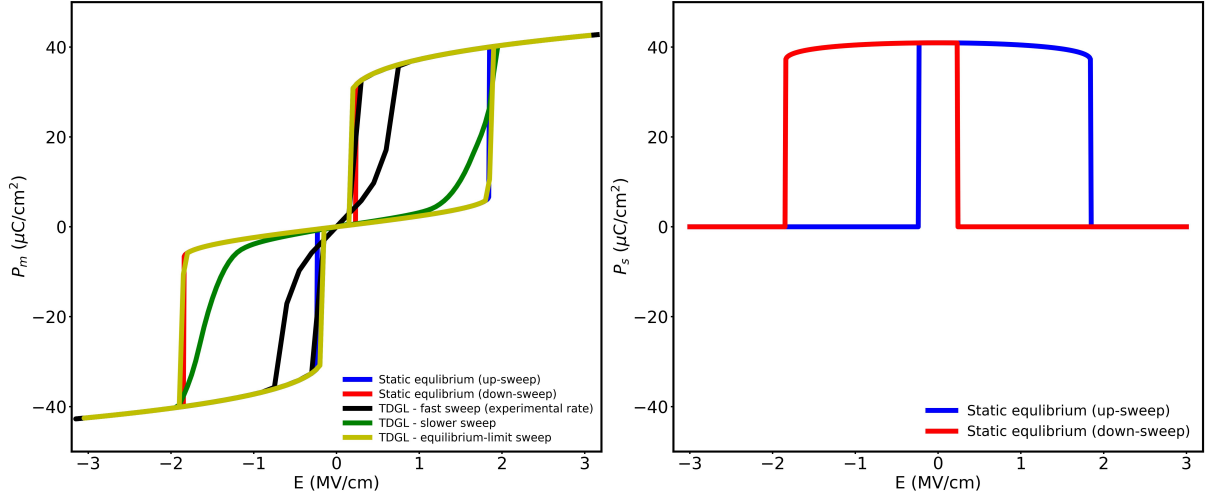


Figure 3: TDGL switching trajectories compared with the quasi-static equilibrium reference (red/blue). The experimental sweep rate ($\nu = 10$ kHz, black) exhibits kinetic deviation from equilibrium, while slower sweeping (green, yellow) progressively restores antipolar order and converges to the thermodynamic hysteresis loop.

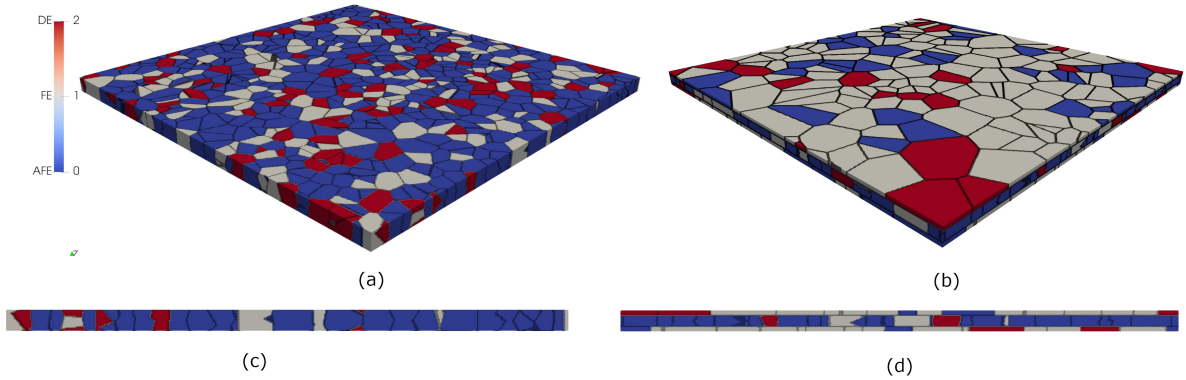


Figure 4: Representative polycrystalline thin-film microstructures used in the TDGL simulations. (a) Single-layer AFE-dominated film with minority FE and DE grains. (b) Multilayer film with vertically segregated phase distributions, consisting of AFE-rich and FE-rich layers. Panels (a,b) show oblique 3-D views, while panels (c,d) show the corresponding $y-z$ cross-sectional views. Grain boundaries are indicated in black. The color scale denotes the phase-ID.

at grain boundaries, deflecting along them, or propagating preferentially through clusters of more easily switchable grains. These effects emerge naturally from the TDGL formulation without invoking explicit grain-boundary mobility models.

Grain sizes are chosen to reflect experimentally observed nanocrystalline regimes. GIXRD measurements on ultrathin ZrO_2 films report coherently diffracting domain sizes of approximately 5–15 nm for thicknesses between 5–20 nm, reflecting crystallite (coherence) lengths rather than physical grain diameters [42]. For polycrystalline $\text{Hf}_{1-x}\text{Zr}_x\text{O}_2$ thin films, experimental studies report laterally extended nanocrystalline grains with characteristic length scales on the order of ~ 30 nm over a broad range of Zr compositions, spanning FE- and AFE-dominated electrical responses [43]. Based on these observations, we target a mean in-plane grain size of approximately 30–35 grid points (30–35 nm for $l_0 = 1$ nm) by using about 800 grains in a $940 \times 940 \times 10$ grid. In multilayer films, grains are distributed among layers in proportion to layer thickness to maintain comparable mean grain sizes and layer-confined morphologies. Thicker layers therefore contain a larger number of grains without introducing structural bias.

Throughout the TDGL simulations, grain morphology, phase assignment, phase fractions, simulation parameters, are prescribed a priori and remain unchanged. This reflects the experimental context of electric-field-driven switching in which grain structures are effectively immobile and microstructural evolution (e.g., grain growth or grain-boundary migration) occurs on much longer timescales. The analysis therefore focuses exclusively on polarization dynamics within a static polycrystalline network.

4.3 Grain-resolved switching microstructures in polycrystalline single-layer AFE films

For the calibrated AFE P – E switching response shown in Fig. 2b, we examine the corresponding grain-resolved polarization microstructures. Fig. 5 shows such microstructures in global-frame during electric-field sweeping at two characteristic points along the P – E curve: the maximum applied electric field ($E = +E_{\max}$), corresponding to the field-induced polar state, and zero field after reversal ($E = 0$), corresponding to recovery of the antipolar ground state. The configuration at $E = -E_{\max}$ is symmetry-equivalent and is therefore not shown. Identical color scales (in $\mu\text{C}/\text{cm}^2$) are used for all polarization microstructure figures unless otherwise specified.

Although all grains share identical AFE Landau coefficients, crystallographic misorientation introduces pronounced spatial heterogeneity, resulting in non-uniform switching through distributed nucleation, partial suppression of antipolar order under applied electric fields, and recovery of antipolar domains upon field reversal. Polarization microstructures of 100% FE film (Fig. 2a) are shown in Fig. S2. In that case, $P_{s,z}$ remains identically zero throughout the field cycle.

At $E = +E_{\max}$, $P_{m,z}^G$ approaches a near-saturated value $40\mu\text{C}/\text{cm}^2$ [Fig. 5(a)], indicating a field-stabilized FE-like state. $P_{s,z}^G$ is strongly reduced but remains finite [Fig. 5(b)], despite the absence of any intrinsically FE phase. This residual antipolar signal reflects incomplete suppression of antipolar order arising from grain-scale heterogeneity rather than a uniform destabilization of the AFE state.

Upon field reversal at $E = 0$, $P_{m,z}$ collapses nearly everywhere (Fig. 5(c)), reflecting the absence of P_r in a purely AFE system. Such reversible field-induced polar states have been observed experimentally in ultrathin ZrO_2 films, where confinement and processing conditions suppress the tetragonal-to-monoclinic transformation and stabilize a tetragonal-to-orthorhombic switching pathway [7, 44]. In contrast, $P_{s,z}^G$ recovers strongly and forms extended antipolar domain patterns [Fig. 5(d)], indicating restoration of the AFE ground state.

Comparison with local-frame polarization fields (Fig. S3) reveals that the residual $P_{s,z}^G$ at E_{\max} arises from projection and incomplete cancellation of locally saturated antipolar domains across misoriented grains, rather than suppression of the intrinsic AFE order. These results demonstrate that strong electric fields drive a nominally single-phase AFE polycrystalline film into a reversible field-induced polar state, while antipolar order persists locally and fully recovers upon unloading. The macroscopic P – E response therefore emerges from the collective behavior of crystallographically distinct grains, underscoring the importance of explicitly resolving microstructural effects when interpreting experimental switching characteristics. Similar grain-mediated disruption and recovery of antipolar order have been exploited in Pb-based perovskite AFEs to tailor hysteresis and energy storage performance [13, 14].

4.4 Influence of phase fractions on macroscopic switching response

To connect the phase-field simulations with experimentally observed P – E trends, we adopt representative phase fractions reported for HZO thin films by Mittmann *et al.* [45]. These experimentally inferred

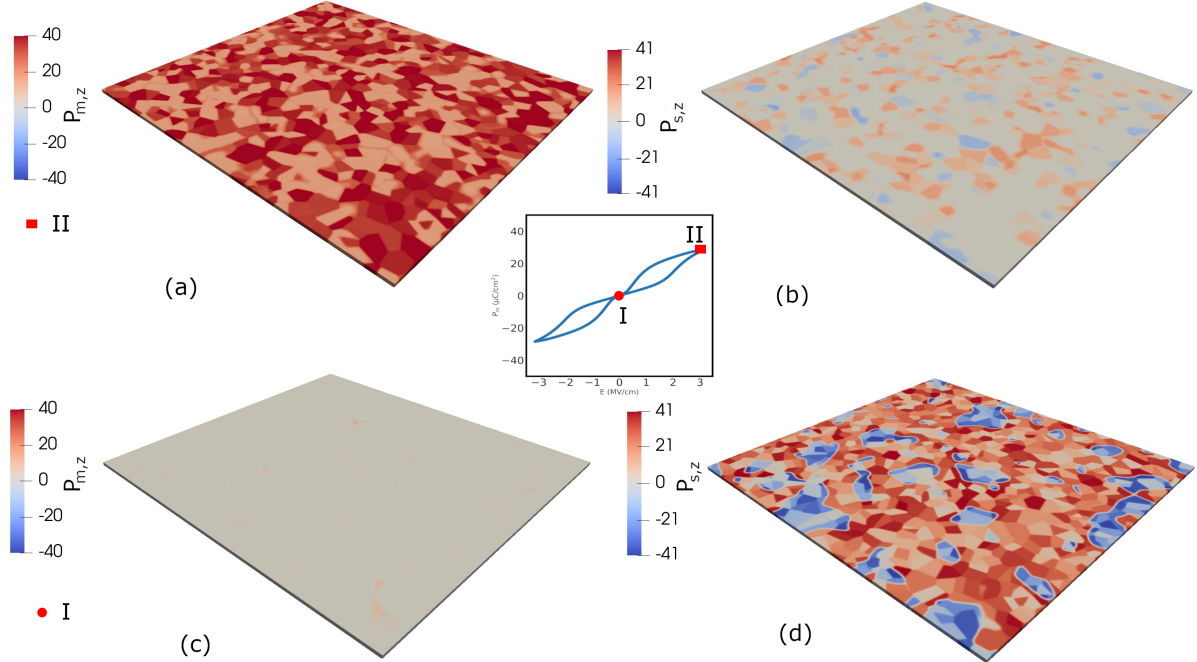


Figure 5: Global-frame polarization microstructures in a 100% AFE single-layer polycrystalline film. Panels (a,b) show $P_{m,z}^G$ and $P_{s,z}^G$ at $E = +E_{\max}$, and panels (c,d) show the corresponding fields at $E = 0$ after field reversal.

fractions are: (A) 60% AFE–35% FE–5% DE, (B) 15% AFE–75% FE–10% DE, and (C) 5% AFE–25% FE–70% DE. In the present simulations, these phase fractions are treated as prescribed input parameters, while intrinsic phase thermodynamics are represented by fixed Landau coefficients (see Section 3.2). This approach isolates microstructure- and architecture-driven switching effects. For each case, phase identities are randomly assigned to grains according to the prescribed fractions. The resulting simulated P – E loops are shown in Fig. 6.

When the AFE phase dominates (A), the P – E loop remains pinched at $E = 0$ with low P_r , indicating some recovery of P_s upon field reversal, in line with experimentally inferred thermodynamic scenarios for pinched hysteresis in ZrO_2 - and HfO_2 -based films [30]. As the FE fraction increases (B), the response evolves toward a FE-like hysteresis with finite remanence, although P_r remains reduced relative to 100% FE film due to AFE and DE phases. When the DE phase dominates (C), both remanent and saturation polarizations are further suppressed, reflecting dilution of switchable polar regions and an increased contribution from linear dielectric response.

Overall, the simulated P – E curves show similar trends as reported by Mittmann *et al.* [45], demonstrating that the macroscopic switching response is governed primarily by relative phase fractions rather than by specific chemical mechanisms or additional effects not explicitly included in the model.

4.5 Vertical phase architectures in polycrystalline thin films

We next examine whether vertical phase arrangement provides an additional degree of control over E_c and P_r . To this end, we systematically compare single-layer and multilayer architectures under otherwise identical conditions, isolating the effect of vertical phase segregation from compositional influences.

Single-layer films consist of mixed AFE and FE grains distributed throughout the full film thickness, producing fully 3-D equiaxed grains with grain boundaries extending in all spatial directions. Electrical coupling to the electrodes therefore occurs through percolative pathways within a heterogeneous grain network, and these films serve as the reference.

Multilayer films are constructed by vertically segregating phases along the film normal. Two classes are considered. In double-layer architectures, an AFE-rich layer contacts the bottom electrode and is capped by an FE-rich layer, resulting in asymmetric electrode–phase contact. In triple-layer architectures, the AFE-rich layer is confined to the film interior and sandwiched between FE-rich layers that contact both electrodes, preserving symmetric electrode contact while isolating the AFE phase from the

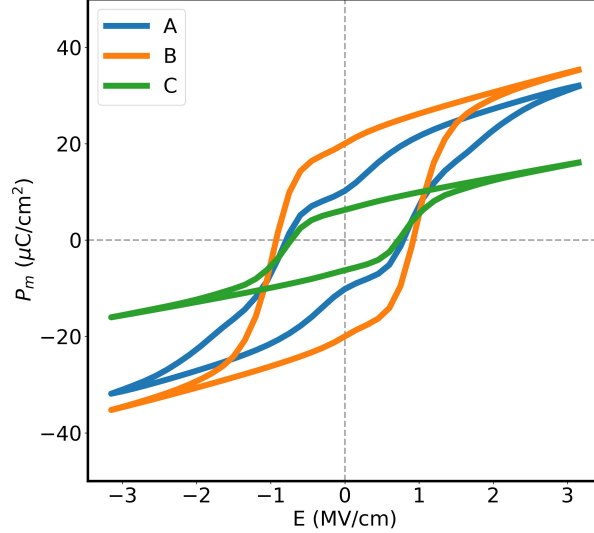


Figure 6: Simulated P – E loops for single-layer polycrystalline films using experimental-informed phase fractions from Ref. [45]: (A) 60% AFE–35% FE–5% DE, (B) 15% AFE–75% FE–10% DE, and (C) 5% AFE–25% FE–70% DE.

interfaces. A schematic overview of the architectures is shown in Fig. 7, and a representative polycrystalline film architecture is shown in Fig. 4.

The total film thickness, phase identity, and grain-size statistics are kept identical across all architectures. In multilayer films, the placement of an AFE-rich region is systematically varied relative to the electrodes without altering the intrinsic properties of the FE-dominated material. This controlled design space enables direct evaluation of the influence of vertical phase distribution on P_r and E_c . Internal FE–AFE interfaces influence switching through local electrostatic and kinetic coupling, represented here in a minimal phenomenological manner, such that observed trends reflect geometry- and coupling-driven effects rather than changes in intrinsic material composition. Phase fractions for all architectures are summarized in Table 2.

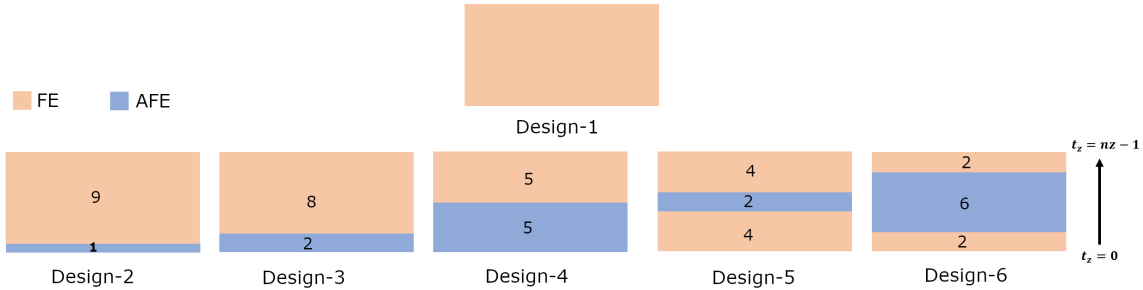


Figure 7: Schematic illustration of the polycrystalline thin-film architectures considered in this study: Design-1 shows the single-layer configuration, Designs-2–4 correspond to double-layer architectures, and Designs-5–6 represent triple-layer architectures. Numbers indicate relative layer thicknesses (grid units) along the film-normal direction.

Table 2: Phase fractions used in the polycrystalline thin-film architectures.

Design type	AFE fraction (%)	FE fraction (%)
Single-layer (Baseline 1)	10	90
Single-layer (Baseline 2)	30	70
FE-rich layer (multilayer)	10 or 30	90 or 70
AFE-rich layer (multilayer)	60	40

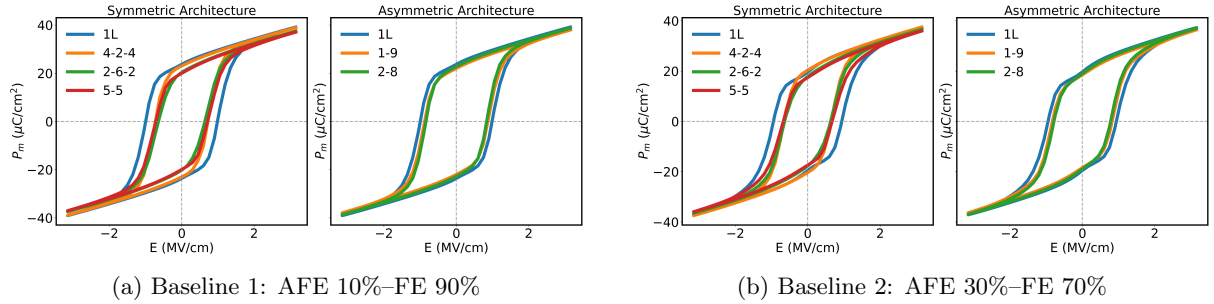


Figure 8: P – E response of polycrystalline thin films for the single-layer and multilayer architectures. (a) Architectures with FE-rich layers having Baseline 1 phase fractions. (b) Architectures with FE-rich layers having Baseline 2 phase fractions.

4.5.1 Macroscopic switching response of multilayer architectures

Fig. 8 compares the P – E response of the two single-layer baseline films and the different multilayer architectures. These P – E curves correspond to a single grain-topology realization; statistical variability across multiple realizations is quantified in the next subsection. As shown in Section 4.4, both single-layer films exhibit predominantly FE-like single hysteresis loops despite the presence of a finite AFE fraction. Introducing vertical phase segregation through multilayer architectures systematically modifies the P – E response. In particular, films containing an AFE-dominated layer exhibit reduced loop area relative to the baseline films, motivating a quantitative comparison of P_r and E_c . Notably, all multilayer architectures retain a single, continuous hysteresis loop without typical AFE double hysteresis. This indicates that the AFE-dominated layer does not switch independently but instead modulates the macroscopic response through electrostatic and kinetic coupling to surrounding FE-rich regions. Such behavior is seen in prior phase-field studies, which report preferential FE domain nucleation at AFE domain boundaries and suppression of saturation polarization through interfacial coupling in AFE-containing structures [46, 47]. Vertical phase placement therefore manifests primarily as systematic shifts in P_r and E_c , while preserving an overall FE-like switching character. A stronger AFE-rich layer (e.g., 90% AFE) would further reduce E_c while also suppressing P_r , leading to poor polarization retention at $E = 0$. Such sensitivity of AFE switching pathways to electrostatic boundary conditions and layer stacking has been demonstrated experimentally in dielectric/AFE heterostructures that stabilize otherwise unstable polarization states in zirconia-based films [32].

4.5.2 Quantitative analysis of remanent polarization and coercive field

To quantitatively assess the influence of vertical phase distribution on switching behavior, we extract P_r and E_c from the P – E loops shown in Fig. 8. For each architecture, P_r and E_c are evaluated separately for positive and negative field sweeps and then averaged to obtain representative values,

$$P_{r,\text{avg}} = \frac{1}{2} (|P_r^+| + |P_r^-|), \quad E_{c,\text{avg}} = \frac{1}{2} (|E_c^+| + |E_c^-|), \quad (15)$$

where superscripts + and – denote quantities extracted from the positive and negative field branches, respectively. These averaged metrics provide a representative measure of intrinsic switching behavior while minimizing the influence of minor loop asymmetries.

Fig. 9 summarizes $P_{r,\text{avg}}$ and $E_{c,\text{avg}}$ for all polycrystalline architectures. Each data point represents the mean value obtained from multiple independent grain-topology realizations, and the error bars denote the corresponding standard deviation, thereby quantifying the variability arising from stochastic Voronoi microstructures. For both baseline fractions, the single-layer films exhibit the largest $P_{r,\text{avg}}$ and $E_{c,\text{avg}}$. Introducing an AFE-dominated layer in multilayer architectures leads to a systematic reduction in both quantities. Notably, the reduction in $E_{c,\text{avg}}$ is consistently more pronounced than that in $P_{r,\text{avg}}$, indicating that the primary role of the AFE-rich layer is to lower the effective switching field rather than to strongly modify $P_{r,\text{avg}}$. The numerical values corresponding to Fig. 9 are provided in Tables S1 and S2.

Experimental studies on FE/AFE sandwich-stacked HfO_2 -based thin films have similarly reported substantial reductions in E_c in multilayer architectures, with some stacks also exhibiting enhanced P_r [48]. In the present simulations, vertical phase arrangement robustly reduces E_c through electrostatic and kinetic coupling between FE-rich and AFE-rich layers, but does not generically enhance P_r .

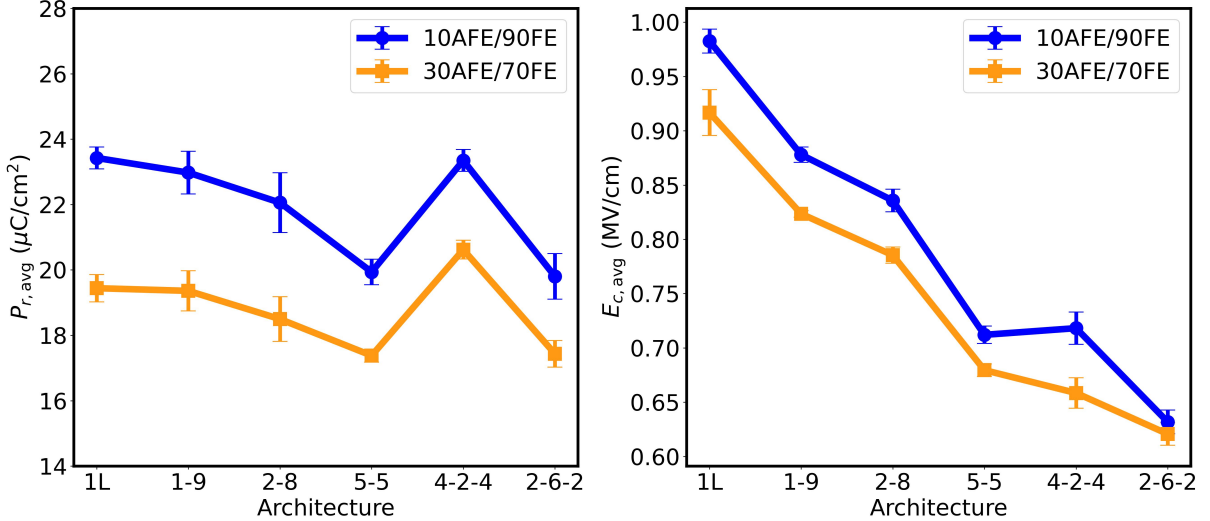


Figure 9: Average remanent polarization $P_{r,\text{avg}}$ and coercive field $E_{c,\text{avg}}$ for polycrystalline thin films with different vertical phase distributions. Symbols denote mean values obtained from multiple grain-topology realizations, and error bars indicate one standard deviation reflecting microstructural.

This reflects the absence of interface- or chemistry-driven AFE \rightarrow FE phase conversion during electric-field cycling. Consequently, P_r is governed primarily by the volume fraction and connectivity of FE-rich layers, whereas vertical stacking mainly reshapes switching pathways rather than the zero-field ground state. Additional interface-, dopant-, or processing-induced phase stabilization mechanisms are therefore likely required to achieve substantial P_r enhancement beyond the architecture-only effects captured here; explicit incorporation of defect-mediated electrostatic and transport effects will be addressed in future work.

Among symmetric multilayer architectures, increasing the thickness of the AFE-dominated layer reduces both $P_{r,\text{avg}}$ and $E_{c,\text{avg}}$, reflecting the growing volume fraction of AFE-rich material that resists ferroelectric switching and redistributes the applied electric field. In contrast, asymmetric multilayer architectures partially preserve $P_{r,\text{avg}}$ while still achieving a substantial reduction in $E_{c,\text{avg}}$, yielding a more favorable trade-off between polarization retention and switching field. Across all multilayer configurations, the reduction in $E_{c,\text{avg}}$ persists despite moderate statistical variability, suggesting that the trend is linked to the imposed vertical phase arrangement rather than stochastic grain connectivity. In the following, we analyze the grain-scale switching pathways responsible for these trends, before distilling general design principles.

4.5.3 Grain-resolved switching mechanisms and design implications

To identify the microscopic origin of the reduced E_c , we analyze grain-resolved switching pathways for architectures having Baseline 1 fractions, focusing on a symmetric 2–6–2 (largest E_c reduction) and an asymmetric 1–9 (strongest vertical asymmetry). Baseline 2 architectures show similar behavior and are omitted for brevity. Because E_c differs between architectures, snapshots are aligned by switching events rather than applied-field values, enabling direct comparison of nucleation, percolation, and system-spanning reversal.

Six snapshots are extracted at equivalent stages of the hysteresis cycle (Fig. 10): (a) $+E_{\text{max}}$ saturation, (b) positive remanence at $E = 0$, (c,d) the coercive window bracketing macroscopic reversal, (e) $-E_{\text{max}}$ saturation, and (f) negative remanence at $E = 0$. The coercive window shifts from $E = -0.90/ -1.05$ MV/cm in the single-layer film (Fig. 10(a)-3,4), to $E = -0.75/ -0.90$ MV/cm in the asymmetric multilayer (Fig. 10(c)-3,4), and to $E = -0.60/ -0.75$ MV/cm in the symmetric multilayer (Fig. 10(b)-3,4), reproducing the hierarchy of E_c values in Fig. 9a.

Such separation between single-domain and multidomain switching fields has also been reported in atomic-scale simulations of AFE PbZrO_3 , highlighting the role of domain structures and electrostatic boundary conditions in lowering the effective switching field [49, 50]. In both those studies, switching proceeds via local collapse and reconfiguration of antipolar order, with strongly pinned domain walls, rather than through uniform domain-wall glide. The resulting reduction in E_c thus originates from

earlier nucleation and faster percolation of reversed regions. Such domain-structure-assisted switching is a generic consequence of polarization instabilities in ferroic systems, where electrostatic and gradient energies favor multidomain pathways [51].

In the single-layer Baseline 1 film, polarization reversal initiates through spatially isolated switched clusters at $E = -0.90$ MV/cm (Fig. 10(a)-3), with a system-spanning reversed network forming only at $E = -1.05$ MV/cm (Fig. 10(a)-4), resulting in the largest E_c . Such nucleation-and-growth-dominated switching mediated by grain boundaries is characteristic of FE polycrystals [52]. By contrast, the symmetric 2–6–2 architecture exhibits earlier nucleation at $E = -0.60$ MV/cm (Fig. 10(b)-3), followed by rapid formation of connected reversed pathways at a slightly higher field (Fig. 10(b)-4), yielding the lowest E_c among all configurations. The asymmetric 1–9 architecture shows intermediate behavior, with earlier nucleation than the single-layer film at $E = -0.75$ MV/cm (Fig. 10(c)-4), but less uniform connectivity, leading to complete reversal only at $E = -0.90$ MV/cm (Fig. 10(c)-4). This reflects orientation-dependent switching heterogeneity induced by the asymmetric placement of the AFE-rich layer [53].

The spatial progression of switching can be quantified by the reversed-volume fraction $f_{\text{rev}} = V(P_{m,z} < 0)/V_{\text{tot}}$. Table 3 shows that the increase in f_{rev} across the coercive window is largest for the symmetric multilayer, followed by the asymmetric multilayer and the single-layer film. The larger reversed fractions at comparable switching stages confirm that macroscopic reversal occurs at a lower percolation threshold in multilayer architectures.

Table 3: Reversed-volume fraction f_{rev} evaluated at equivalent, event-aligned stages of the hysteresis cycle for different film architectures.

Design	$+E_{\text{max}}$	$E = 0, +\text{rem}$	pre-rev	post-rev	$-E_{\text{max}}$	$E = 0, -\text{rem}$
	f_{rev}	f_{rev}	f_{rev}	f_{rev}	f_{rev}	f_{rev}
1L	0.00	1.58	28.21	45.41	100.00	97.24
2–6–2	0.00	0.50	38.47	56.66	100.00	98.92
1–9	0.00	1.27	25.06	43.00	100.00	98.11

Across all architectures, E_c is governed by the field required to establish a connected, system-spanning reversed network rather than by isolated local nucleation events, as reported in prior grain-resolved phase-field studies of ferroelectric polycrystals [52, 53]. Multilayer architectures reduce E_c by enabling earlier nucleation and more rapid percolation of reversed regions, reflecting the general tendency of multidomain switching pathways to lower effective switching fields in antiferroelectrics [49]. Remanent snapshots in Fig. 10 further reveal increased polarization heterogeneity at zero field in multilayer films. For Baseline 1, this heterogeneity suppresses polarization retention, whereas for Baseline 2, selected multilayers—most notably the symmetric 4–2–4—slightly exceed the single-layer P_r while still exhibiting a reduced E_c (Fig. 9).

Design principles for FE–AFE polycrystalline heterostructures (Fig. 7)

- **Vertical phase segregation reduces E_c .** Introducing an AFE-dominated layer within an FE-rich polycrystalline film lowers E_c through electrostatic and kinetic coupling, without activating independent AFE switching.
- **Interior placement of the AFE layer is most effective.** Symmetric multilayer architectures with the AFE-rich layer confined to the film interior facilitate earlier percolation of reversed domains and yield the largest reduction in E_c , whereas asymmetric architectures provide a more moderate reduction.
- **P_r is set by FE-rich layers.** The remanent polarization P_r is governed primarily by the phase fraction and connectivity of FE-rich layers and cannot be enhanced by vertical arrangement alone.
- **Optimal performance requires a balanced AFE fraction.** Moderately AFE-rich interior layers (e.g., 60% AFE) provide a favorable trade-off between reduced E_c and retained P_r , while higher AFE fractions further lower E_c at the expense of polarization retention.

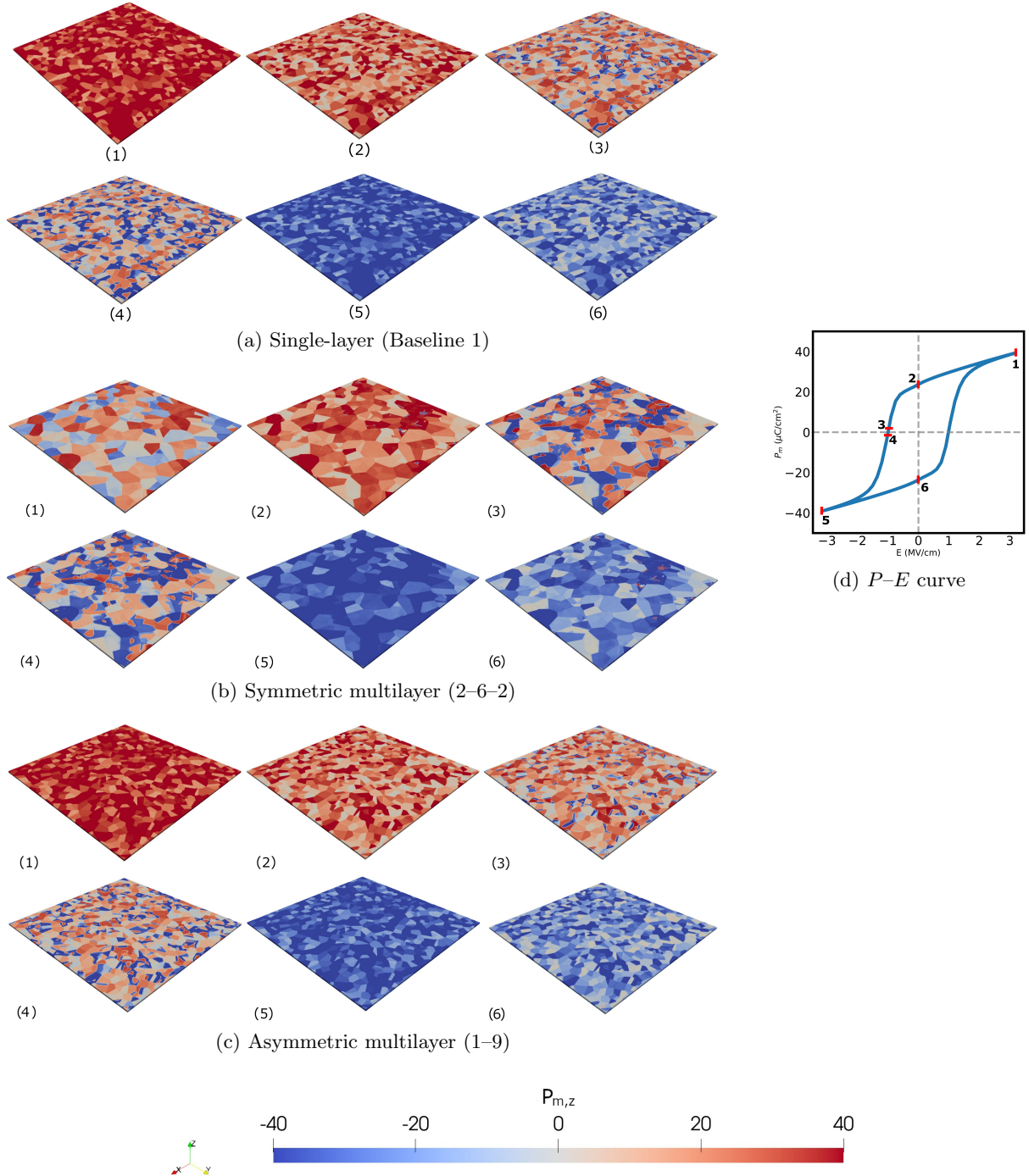


Figure 10: Grain-resolved switching snapshots of $P_{m,z}$. Panels (1–6) in each sub-figure correspond to equivalent, event-aligned stages marked on the P - E curve.

5 Conclusion

We developed a unified grain-resolved, 3-D phase-field framework to investigate electric-field-driven switching in polycrystalline hafnia-based thin films with mixed FE, AFE, and DE phases. The model explicitly resolves realistic 3-D grain topology, crystallographic orientation, and antipolar sublattice kinetics by evolving both macroscopic and staggered polarization order parameters, while adopting a uniaxial capacitor formulation with self-consistent depolarization fields. All thermodynamic and kinetic parameters were calibrated to experimental P – E data and held fixed, enabling direct isolation of microstructural and architectural effects.

The simulations show that polycrystallinity fundamentally reshapes AFE switching by promoting domain-structure-assisted pathways that reduce E_c relative to single-crystal thermodynamic limits. In nominally single-phase AFE polycrystals, strong fields stabilize a reversible FE-like state while antipolar order persists locally due to crystallographic misorientation, showing AFE \rightarrow FE transition. For mixed-phase single-layer films, the variation of P_r and E_c with phase fraction broadly follows experimentally observed trends, suggesting that the macroscopic switching response is governed primarily by phase distribution rather than by specific chemical stabilization mechanisms.

Vertical phase arrangement provides an additional and effective control knob to tailor P_r and E_c . Introducing an AFE-dominated layer within an FE-rich polycrystalline film reduces E_c more strongly than P_r , while preserving a single, continuous FE-like hysteresis loop and avoiding independent AFE switching. Grain-resolved analysis reveals that this reduction in E_c originates from earlier nucleation and accelerated percolation of reversed domains across the film thickness. Symmetric three-layer architectures with an interior AFE-rich layer maximize this cooperative effect, whereas asymmetric stacks yield intermediate trade-offs.

These results help in establishing clear design principles for FE–AFE hafnia heterostructures under fixed thickness and identical electrical loading: vertical phase segregation enables substantial coercive-field reduction without severe remanence loss, interior placement of moderately AFE-rich layers is optimal, and multilayer architectures can be exploited to engineer switching behavior beyond what is achievable in single-layer polycrystalline films. Thus, the proposed model provides a predictive platform for phase-engineered hafnia-based ferroelectric capacitors.

Beyond its immediate application to ferroic switching physics, the present phase-field framework provides a physics-consistent basis for generating high-fidelity datasets describing polarization evolution, domain interactions, and microstructure-dependent switching behavior in mixed-phase hafnia thin films. Such datasets can enable the development of data-driven surrogate models, including graph neural networks [29] and neural-operator approaches [54], for accelerated exploration of microstructure–property relationships. Detailed results from these efforts will be reported in future studies.

Declaration of Competing Interest

The authors declare that they have no known competing financial interests or personal relationships that could have appeared to influence the work reported in this paper.

Acknowledgments

This work was supported by the National Research Foundation of Korea (NRF) funded by the Ministry of Science and ICT through the Nano & Material Technology Development Program (RS-2024-00444182) and another NRF grant (RS-2024-00450836).

References

- [1] G. Catalan, Switching on antiferroelectrics, arXiv preprint arXiv:2503.20423 (2015).
- [2] Z. Liu, T. Lu, J. Ye, G. Wang, X. Dong, R. Withers, Y. Liu, Antiferroelectrics for energy storage applications: a review, *Advanced Materials Technologies* 3 (9) (2018) 1800111.
- [3] M. Pešić, M. Hoffmann, C. Richter, T. Mikolajick, U. Schroeder, Nonvolatile random access memory and energy storage based on antiferroelectric like hysteresis in ZrO_2 , *Advanced Functional Materials* 26 (41) (2016) 7486–7494.

[4] C. A. Randall, Z. Fan, I. Reaney, L.-Q. Chen, S. Trolier-McKinstry, Antiferroelectrics: History, fundamentals, crystal chemistry, crystal structures, size effects, and applications, *Journal of the American Ceramic Society* 104 (8) (2021) 3775–3810.

[5] Y. Si, T. Zhang, C. Liu, S. Das, B. Xu, R. G. Burkovsky, X.-K. Wei, Z. Chen, Antiferroelectric oxide thin-films: Fundamentals, properties, and applications, *Progress in Materials Science* 142 (2024) 101231.

[6] T. S. Böscke, J. Müller, D. Bräuhaus, U. Schröder, U. Böttger, Ferroelectricity in hafnium oxide thin films, *Applied Physics Letters* 99 (10) (2011) 102903.

[7] J. Müller, T. S. Böscke, U. Schröder, S. Mueller, D. Bräuhaus, U. Böttger, L. Frey, T. Mikolajick, Ferroelectricity in simple binary ZrO_2 and HfO_2 , *Nano Letters* 12 (8) (2012) 4318–4323, PMID: 22812909.

[8] M. H. Park, Y. H. Lee, H. J. Kim, Y. J. Kim, T. Moon, K. D. Kim, J. Müller, A. Kersch, U. Schroeder, T. Mikolajick, C. S. Hwang, Ferroelectricity and antiferroelectricity of doped thin HfO_2 -based films, *Advanced Materials* 27 (11) (2015) 1811–1831.

[9] Z. Weng, L. Zhao, C. Lee, Y. Zhao, Phase transitions and anti-ferroelectric behaviors in $Hf_{1-x}Zr_xO_2$ films, *IEEE Electron Device Letters* 44 (10) (2023) 1780–1783.

[10] S. Yan, P. Xu, G. Li, Y. Zhu, Y. Wu, Q. Chen, S. Liu, Q. Li, M. Tang, Phase transition mechanism and property prediction of hafnium oxide-based antiferroelectric materials revealed by artificial intelligence, *Journal of Materomics* 11 (4) (2025) 100968.

[11] H. Gao, X. Hao, Q. Zhang, S. An, L. B. Kong, Electrocaloric effect and energy-storage performance in grain-size-engineered pblzt antiferroelectric thick films, *Journal of Materials Science: Materials in Electronics* 27 (10) (2016) 10309–10319.

[12] Z. Liu, B.-X. Xu, Insight into perovskite antiferroelectric phases: Landau theory and phase field study, *Scripta Materialia* 186 (2020) 136–141.

[13] Y. Zhou, T. Zhang, L. Chen, H. Yu, R. Wang, H. Zhang, J. Wu, S. Deng, H. Qi, C. Zhou, et al., Design of antiferroelectric polarization configuration for ultrahigh capacitive energy storage via increasing entropy, *Nature Communications* 16 (1) (2025) 805.

[14] B. Yang, Y. Liu, R.-J. Jiang, S. Lan, S.-Z. Liu, Z. Zhou, L. Dou, M. Zhang, H. Huang, L.-Q. Chen, et al., Enhanced energy storage in antiferroelectrics via antipolar frustration, *Nature* 637 (8048) (2025) 1104–1110.

[15] L. D. Geng, Y. M. Jin, D. Q. Tan, Y. U. Wang, Computational study of nonlinear dielectric composites with field-induced antiferroelectric-ferroelectric phase transition, *Journal of Applied Physics* 124 (16) (2018) 164109.

[16] D. Chen, S. Zhong, Y. Dong, T. Cui, J. Liu, M. Si, X. Li, Antiferroelectric phase evolution in $Hf_xZr_{1-x}O_2$ thin film toward high endurance of non-volatile memory devices, *IEEE Electron Device Letters* 43 (12) (2022) 2065–2068.

[17] S.-C. Chang, K. Chae, M. I. Popovici, C.-C. Lin, S. Siddiqui, I.-C. Tung, J. Bizindavyi, B. G. Alpizar, N. Haratipour, M. Metz, J. Kavalieros, G. S. Kar, A. Kummel, K. Cho, U. E. Avci, Multi-domain phase-field modeling of polycrystalline hafnia-based (anti-)ferroelectrics capable of representing defects, wake-up and fatigue, in: 2022 International Electron Devices Meeting (IEDM), 2022, pp. 13.1.1–13.1.4.

[18] M. M. Islam, M. Adnaan, S.-C. Chang, H. Li, I. A. Young, A. Naeemi, Investigating the switching dynamics of antiferroelectric capacitor using multidomain phase-field approach, *IEEE Journal of the Electron Devices Society* 13 (2025) 422–426.

[19] M. H. Park, Y. H. Lee, H. J. Kim, T. Schenk, W. Lee, K. D. Kim, F. P. G. Fengler, T. Mikolajick, U. Schroeder, C. S. Hwang, Surface and grain boundary energy as the key enabler of ferroelectricity in nanoscale hafnia-zirconia: a comparison of model and experiment, *Nanoscale* 9 (2017) 9973–9986.

[20] R. Ganser, P. D. Lomenzo, L. Collins, B. Xu, L. A. Antunes, T. Mikolajick, U. Schroeder, A. Kersch, Mechanism of antiferroelectricity in polycrystalline ZrO_2 , *Advanced Functional Materials* 34 (40) (2024) 2405513.

[21] C. Kittel, Theory of antiferroelectric crystals, *Phys. Rev.* 82 (1951) 729–732.

[22] K. M. Rabe, *Antiferroelectricity in Oxides: A Reexamination*, John Wiley & Sons, Ltd, 2013, Ch. 7, pp. 221–244.

[23] C. Y. Lum, K.-G. Lim, K.-H. Chew, Revisiting the kittel's model of antiferroelectricity: phase diagrams, hysteresis loops and electrocaloric effect, *Journal of Physics: Condensed Matter* 34 (41) (2022) 415702.

[24] L. Cross, Antiferroelectric-ferroelectric switching in a simple “kittel” antiferroelectric, *Journal of the Physical Society of Japan* 23 (1) (1967) 77–82.

[25] M. Lederer, T. Kämpfe, R. Olivo, D. Lehninger, C. Mart, S. Kirbach, T. Ali, P. Polakowski, L. Roy, K. Seidel, Local crystallographic phase detection and texture mapping in ferroelectric Zr doped HfO_2 films by transmission-ebsd, *Applied Physics Letters* 115 (22) (2019) 222902.

[26] R. Koduru, A. K. Saha, M. M. Frank, S. K. Gupta, Small-signal capacitance in ferroelectric hafnium zirconium oxide: mechanisms and physical insights, *Nanoscale* 17 (2025) 6154–6170.

[27] S. B. Vakhrushev, D. Andronikova, I. Bronwald, E. Y. Koroleva, D. Chernyshov, A. V. Filimonov, S. A. Udovenko, A. I. Rudskoy, D. Ishikawa, A. Q. R. Baron, A. Bosak, I. N. Leontiev, A. K. Tagantsev, Electric field control of antiferroelectric domain pattern, *Phys. Rev. B* 103 (2021) 214108.

[28] S. Sugathan, K. Thekkepat, S. Bandyopadhyay, J. Kim, P.-R. Cha, A phase field model combined with a genetic algorithm for polycrystalline hafnium zirconium oxide ferroelectrics, *Nanoscale* 14 (2022) 14997–15009.

[29] A.-L. Kévin, D. Damien, G. Brice, Ultrafast and accurate prediction of polycrystalline hafnium oxide phase-field ferroelectric hysteresis using graph neural networks, *Nanoscale Advances* 6 (9) (2024) 2350–2362.

[30] P. D. Lomenzo, M. Materano, C. Richter, R. Alcala, T. Mikolajick, U. Schroeder, A Gibbs energy view of double hysteresis in ZrO_2 and si-doped HfO_2 , *Applied Physics Letters* 117 (14) (2020) 142904.

[31] M. Segatto, F. Rupil, D. Esseni, Analytical procedure for the extraction of material parameters in antiferroelectric ZrO_2 , *IEEE Transactions on Electron Devices* 70 (6) (2023) 3037–3042.

[32] M. Hoffmann, Z. Wang, N. Tasneem, A. Zubair, P. V. Ravindran, M. Tian, A. A. Gaskell, D. Triyoso, S. Consiglio, K. Tapily, et al., Antiferroelectric negative capacitance from a structural phase transition in zirconia, *Nature communications* 13 (1) (2022) 1228.

[33] X. Ke, D. Wang, X. Ren, Y. Wang, Polarization spinodal at ferroelectric morphotropic phase boundary, *Phys. Rev. Lett.* 125 (2020) 127602.

[34] X. Tan, J. Frederick, C. Ma, E. Aulbach, M. Marsilius, W. Hong, T. Granzow, W. Jo, J. Rödel, Electric-field-induced antiferroelectric to ferroelectric phase transition in mechanically confined $Pb_{0.99}Nb_{0.02}[(Zr_{0.57}Sn_{0.43})_{0.94}Ti_{0.06}]_{0.98}O_3$, *Phys. Rev. B* 81 (2010) 014103.

[35] T. R. Kim, A. K. Saha, S. K. Gupta, Analysis of polarization switching in HZO/ ZrO_2 (HZZ) nanolaminates based on sub-lattice phase-field model, in: 2023 Device Research Conference (DRC), 2023, pp. 1–2.

[36] D. Li, X. Meng, E. Zhou, X. Chen, Z. Shen, Q. Guo, Z. Yao, M. Cao, J. Wu, S. Zhang, H. Liu, H. Hao, Ultrahigh energy density of antiferroelectric $PbZrO_3$ -based films at low electric field, *Advanced Functional Materials* 33 (44) (2023) 2302995.

[37] R. Koduru, I. Ahmed, A. K. Saha, X. Lyu, P. Ye, S. K. Gupta, Phase-field simulations of polarization variations in polycrystalline $Hf_{0.5}Zr_{0.5}O_2$ based mfim: Voltage dependence and dynamics, *Journal of Applied Physics* 134 (8) (2023) 084104.

[38] P. D. Lomenzo, M. Materano, T. Mittmann, P. Buragohain, A. Gruverman, T. Kiguchi, T. Mikolajick, U. Schroeder, Harnessing phase transitions in antiferroelectric ZrO_2 using the size effect, *Advanced Electronic Materials* 8 (1) (2022) 2100556.

[39] M. Hyuk Park, H. Joon Kim, Y. Jin Kim, W. Lee, T. Moon, C. Seong Hwang, Evolution of phases and ferroelectric properties of thin $\text{Hf}_{0.5}\text{Zr}_{0.5}\text{O}_2$ films according to the thickness and annealing temperature, *Applied Physics Letters* 102 (24) (2013) 242905.

[40] Y. Si, N. Fan, Y. Dong, Z. Ye, S. Deng, Y. Li, C. Zhou, Q. Zeng, L. You, Y. Zhu, et al., Ideal antiferroelectricity with large digital electrostrain in PbZrO_3 epitaxial thin films, *Nature Communications* 16 (1) (2025) 4263.

[41] J. Wang, S.-Q. Shi, L.-Q. Chen, Y. Li, T.-Y. Zhang, Phase-field simulations of ferroelectric/ferroelastic polarization switching, *Acta Materialia* 52 (3) (2004) 749–764.

[42] N. Tasneem, Y. M. Yousry, M. Tian, M. Dopita, S. E. Reyes-Lillo, J. Kacher, N. Bassiri-Gharb, A. I. Khan, A Janovec-Kay-Dunn-like behavior at thickness scaling in ultra-thin antiferroelectric ZrO_2 films, *Advanced Electronic Materials* 7 (11) (2021) 2100485.

[43] S. J. Kim, J. Mohan, J. S. Lee, H. S. Kim, J. Lee, C. D. Young, L. Colombo, S. R. Summerfelt, T. San, J. Kim, Stress-induced crystallization of thin $\text{Hf}_{1-X}\text{Zr}_X\text{O}_2$ films: The origin of enhanced energy density with minimized energy loss for lead-free electrostatic energy storage applications, *ACS Applied Materials & Interfaces* 11 (5) (2019) 5208–5214.

[44] X. Luo, K. Toprasertpong, M. Takenaka, S. Takagi, Antiferroelectric properties of ZrO_2 ultra-thin films prepared by atomic layer deposition, *Applied Physics Letters* 118 (23) (2021) 232904.

[45] T. Mittmann, M. Materano, S.-C. Chang, I. Karpov, T. Mikolajick, U. Schroeder, Impact of oxygen vacancy content in ferroelectric HZO films on the device performance, in: 2020 IEEE International Electron Devices Meeting (IEDM), 2020, pp. 18.4.1–18.4.4.

[46] J. Zhu, Z. Liu, B. Zhong, Y. Wang, B. Xu, Domain size and charge defects affecting the polarization switching of antiferroelectric domains, *Chinese Physics B* 32 (4) (2023) 047701.

[47] K. Xu, S. Tang, C. Guo, Y. Song, H. Huang, Antiferroelectric domain modulation enhancing energy storage performance by phase-field simulations, *Journal of Materiomics* 11 (3) (2025) 100901.

[48] Y. Yang, W. Xu, D. Huang, M. Shao, Y. Guo, L. Zhao, J. Hou, H. Han, Y. Wu, H. Liu, Y. Yang, T.-L. Ren, A comprehensive study on the sandwich stacking structures of antiferroelectric/ferroelectric doped hafnium oxide, *Applied Physics Letters* 126 (2) (2025) 023504.

[49] Y. Shi, R. Wang, Z. Zhong, Y. Wu, S. Liu, L. Si, R. He, Domain and switching dynamics in antiferroelectric PbZrO_3 : Machine learning molecular dynamics simulation, *Materials Genome Engineering Advances* 3 (2) (2025) e70012.

[50] M. Dawber, P. Chandra, P. B. Littlewood, J. F. Scott, Depolarization corrections to the coercive field in thin-film ferroelectrics, *Journal of Physics: Condensed Matter* 15 (24) (2003) L393.

[51] C. M. Bishop, Domain size control by spinodal decomposition in ferroelectrics, *Acta Materialia* 262 (2024) 119446.

[52] S. Choudhury, Y. Li, C. Krill, L.-Q. Chen, Phase-field simulation of polarization switching and domain evolution in ferroelectric polycrystals, *Acta Materialia* 53 (20) (2005) 5313–5321.

[53] S. Choudhury, Y. Li, C. Krill, L. Chen, Effect of grain orientation and grain size on ferroelectric domain switching and evolution: Phase field simulations, *Acta Materialia* 55 (4) (2007) 1415–1426.

[54] Z. Li, N. Kovachki, K. Azizzadenesheli, B. Liu, K. Bhattacharya, A. Stuart, A. Anandkumar, Fourier neural operator for parametric partial differential equations, *arXiv preprint arXiv:2010.08895* (2020).